Verification Study of Sliding and Overset Grid Method
An Application to Wind Turbine CFD Simulations

Tiago João das Neves Gomes
tiago.gomes.21@tecnico.ulisboa.pt

Instituto Superior Técnico, Universidade de Lisboa, Portugal

November 2021

Abstract

Wind turbines are complex dynamic systems, with coupled effects from multiple fields. More accurate CFD simulations require the motion of the different parts of the structure to be captured, which can be impracticable using only a single grid. On that matter Sliding and Overset Grids are two well-known methods that enable the discretization of the domain with multiple meshes. Since the grids can move relatively to one another, body motion can be incorporated, with successful implementations already existent. Nevertheless, no literature can be found assessing their impact on the solution's accuracy in these flows. Therefore, the goal is to apply Verification procedures to three test cases, so that discretization errors can be probed in isolation and the methods compared. The first is a Poiseuille flow, with known analytical solution, yet inexpensive to test multiple parameters. The second is a novel analytical solution of a wind turbine flow, designed with the Method of Manufactured Solutions. The final test case is the NREL 5MW wind turbine, to test the procedures in a practical scenario. Each test case has a parameter sensitivity test performed, with the respective conclusions used as inputs to the next one. The results suggest that Sliding Grids are suitable to be applied in the CFD simulation of wind turbine rotors, whereas Overset tends to present additional implementation difficulties and higher errors. Moreover, pressure oscillations at the interfaces, due to the mass imbalance introduced by these methods, are found to be minimized with interpolation schemes of at least second order.
Keywords: Sliding Grids, Overset Grids, Verification, Wind Turbines, CFD

1. Introduction

Sliding Grids (SG) and Overset Grids (OG) are two Computational Fluid Dynamics (CFD) methods for discretizing the domain with several sub-grids, with the potential of enabling complex body motion in unsteady simulations. Their fundamental difference lies on the sub-grid placement, fitted into each other (SG) [1, 2] or overlapped (OG) [3, 4], which ends up impacting the information transfer mechanism that couples them.

During the last few years both methods have been especially useful in many areas, including the simulation of floating offshore wind turbines (FOWT), where a Sliding Grid might be used to accommodate the motion of the rotor and an Overset Grid to capture the overall movement of the platform with the ocean waves, as in Tran and Kim [5]. However, very few studies exist comparing SG with OG, despite their versatility and interchangeability in various situations [6, 7]. Even within the available literature, authors tend to mostly focus on practical test cases, with no Verification performed. Instead, they usually aim at assessing modelling errors only, through Validation procedures. Therefore, a detailed analysis is necessary, where the flow analytical solution is known, so that discretization errors can be evaluated in isolation. This analysis should also include a parameter sensitivity test, with the goal of producing a set of good practices when applying these methods in wind turbine CFD simulations.

Therefore, this work will focus in applying Verification procedures [8] on wind turbine related flows. Its structure comprises three test cases. The first is a Poiseuille flow, one of the few analytical solutions of the Navier-Stokes (NS) equations, which is inexpensive to run and enables a large number of parameters to be tested. Next, the solution of a wind turbine flow is designed, based on the Method of Manufactured Solutions, which is then forced to become the exact solution of the flow governing equations - therefore, allowing errors to be assessed in a wind turbine-like flow, resembling its main features. Finally, the CFD aerodynamic analysis of the NREL 5MW [9] rotor is performed, to further test the conclusions obtained with the other test cases and apply both SG and OG techniques in a relevant industrial scenario.

2. Numerical Methods

2.1. ReFRESCO

ReFRESCO [10] is a CFD solver based on a finite-volume discretization with cell-centered collocated variables and unstructured grids, capable of handling hanging nodes. It solves the unsteady, multi-phase and incompressible Reynolds-Averaged Navier-Stokes equations, in addition to turbulence models. Moreover, it has the capability to simulate moving objects through the use of Sliding Grids [2] and more recently the Overset Grids method [4].

2.2. Sliding Grids

Sliding Grids [1] are based on the discretization of the domain with grids fitted into one another, sharing common interfaces, as it is exemplified in Figure 1. This characteristic restricts the sub-grid's motion to simple translation or rotation. Regarding the inter-grid communication process, the technique implemented in ReFRESCO, and used in the present work, is based on Halo Cells (HC) [2].

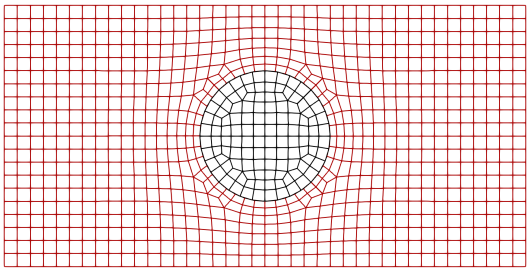

Figure 1: Example of sub-grid placement with Sliding Grids. Domain mesh (red) has hole to fit Circle mesh (black).

The method of Halo Cells, exemplified in Figure 2, projects a virtual cell from one domain into the other. This new cell does not add to the flow's linear system of equations to be solved. Instead, it acts as a Dirichlet boundary condition, as its value is determined by interpolation from a set of neighbour donor cells. The coupling is then satisfied through the calculation of fluxes between the halo and the parent cell. It is important to note that this method does not conserve mass, as the interpolation is performed independently in both directions.

2.3. Overset Grids

The Overset Grids' [3] purpose is similar to SG, but since they only need to overlap, as presented in Figure 3, the requirements for grid generation are looser and the possible motions for the meshes are virtually unlimited.

Nevertheless, that same overlap requires additional treatment, namely the definition of the Do-

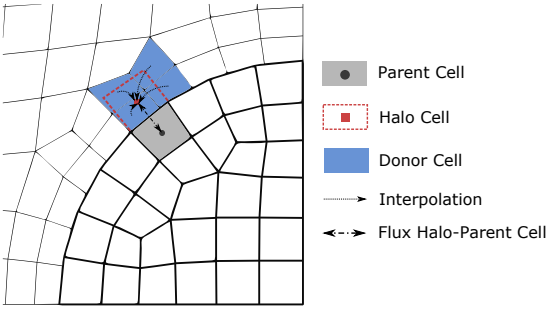

Figure 2: Example of inter-grid communication in Sliding Grids.

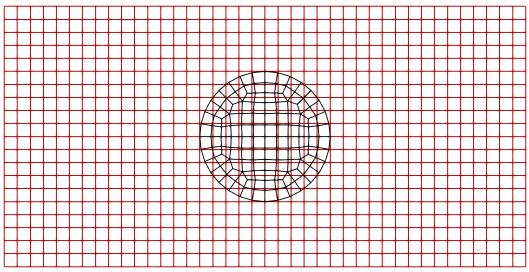

Figure 3: Example of sub-grid placement with Overset Grids. Domain grid (red) is overlapped with Circle mesh (black).

main Connectivity Information (DCI), which assigns to each cell in the domain one of three possible status: *In*, *Fringe* or *Hole* Cell. *In* Cells are regular, active cells in the domain. *Hole* Cells concern the ones that are ignored by the solver, since they are substituted by cells of another sub-grid that is overlapping that region or because they are just outside the domain. Finally, two layers of *Fringe* cells (implementation dependent) are placed in between the two other types of cells, or at the overlapping sub-grid's boundary, to receive the interpolated information from neighbour donor cells and therefore couple the different sub-grids. The vector containing all the cells' status is typically known as IBLANK [3]. An example of this classification is presented in Figure 4.

2.4. Interpolation Schemes

In both SG and OG methods interpolation is necessary to couple the sub-grids. A set of donor cells is assigned for each Halo/Fringe cell, based on the interpolation scheme requirements. A large number of schemes exist, in this work, however, only some of the ones present in ReFRESCO are explored. The reader is referred to the work of Lemaire *et al.* [4] for a more detailed overview of each:

- **Nearest Cell (1st order accurate)**: The in-

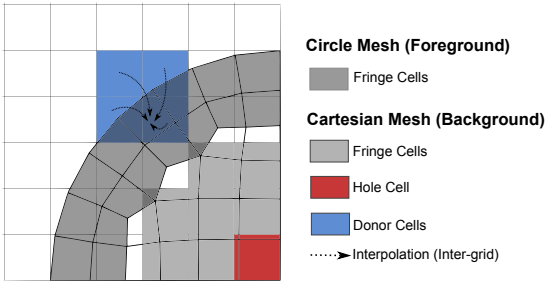

Figure 4: Example of inter-grid communication in Overset Grids.

terpolated quantities have the exact same value as the single donor cell;

- **Inverse Distance (1st order accurate)**: The interpolated value is an average of an arbitrary number of cloud points, weighted with the inverse of the distance to the recipient cell (the farther, the lower the weight);
- **Nearest Cell Gradient (2nd order accurate)**: The interpolated value is calculated based on a Taylor Series expansion, truncated to the first order term. The linear approximation is obtained by using the single donor cell's gradient;
- **Least Squares (n-th order accurate)**: The interpolated value is calculated with a polynomial of degree $n-1$, over defined by a set of donor cells. The resulting system is then solved through least squares minimization, obtaining the polynomial coefficients that best fit the data points. Then, the polynomial value is probed at the recipient cell's center location.

2.5. Verification

The Verification methodologies adopted in the present work are based on the work of Eça and Hoekstra [8]. They aim at assessing if a given set of equations are being solved correctly based on the methods selected and implemented to solve them. Under the concept of Verification, two subcategories exist.

The first is Code Verification, where the error is evaluated by knowing the exact solution, enabling implementation and code errors to be assessed. It is assumed that the error can be described by a power series expansion and that error sources, other than discretization ones, are negligible,

$$\log\left(e(\phi)\right) = \log\left(\alpha\right) + p_{ac}\log\left(h_i\right) \qquad (1)$$

where $e(\phi)$ is the discretization error of a flow quantity ϕ, α the error level, p_{ac} the observed order of accuracy and $h_i = (N_{finest}/N_i)^{1/n}$ the grid refinement level, in which N_i represents the cell count of a mesh and n the number of spatial dimensions. Equation (1) is used to fit a linear equation through the error data points, in the Least Squares sense, in which the obtained slope represents an estimation for p_{ac}. The authors [8] recommend at least four grid refinements to be used.

The second is Solution Verification, where the error is just estimated, which occurs most of the time when no analytical solution is known. It aims at quantifying the accuracy and uncertainty of the obtained solution. For brevity, the uncertainty estimation procedures are not detailed since they are only relevant for the last test case. Yet, the reader is referred to the work of Eça and Hoekstra [8] for more detailed information on the Verification procedures adopted.

2.6. Method of Manufactured Solutions

To perform Code Verification, and probe the errors in the domain, analytical solutions of the flow governing equations are necessary. Nevertheless, that is not possible most of the time, thus why the equations are being solved numerically in the first place. Moreover, while some trivial solutions can be obtained, as the Poiseuille flow in the case of the Navier-Stokes equations, they result from various simplifications. Therefore, many of the terms of the governing equations end up not being exercised.

In order to circumvent this, the Method of Manufactured Solutions (MMS) is proposed, based on the work of Roache [11]. It enables arbitrarily complex flows to become the analytical solution of the governing equations through the following procedure:

1. Design a set of single, continuous functions describing each of the flow quantities of interest;
2. Substitute them in the governing equations, which originates source terms that balance the equations;
3. Provide the source terms to the CFD solver;
4. The initial set of manufactured equations ends up becoming the exact solution of the flow in the CFD simulation, due to the source terms.

Conceptually, this is a very simple method, yet with great potential, since it enables Code Verification of arbitrarily complex flows. It should be noted that since this is a purely mathematical exercise, flow realism is not strictly necessary. However, at least the main features of the target flow should be recreated to ensure that the necessary terms of the governing equations are being activated.

The open-source software pyMMS [12] is used in the present work, which receives as input the set of equations describing the flow quantities, calculates the source terms and outputs a FORTRAN file to be provided to ReFRESCO.

3. Test Cases

In order to compare the SG and OG methods, three test cases are performed: a Poiseuille flow, a Manufactured Solution of a wind turbine flow and the aerodynamic analysis of the rotor of the NREL 5MW wind turbine. These represent flows with progressively resemblance to a wind turbine simulation. At the same time the computational cost also increases, however the preliminary conclusions obtained at the end of each test case are used as inputs to the next one, to narrow down the number of parameters analyzed and therefore save computational resources.

3.1. Poiseuille Flow

The first test case comprises one of the few analytical solutions of the Navier-Stokes equations, the Poiseuille flow [4]. It is a 2D steady flow, driven by an axial pressure gradient, with boundary layer development in between two infinite planes separated by a distance h. In Figure 5 a schematic of the flow's velocity profile can be visualized, including the domain's dimensions and the boundary conditions used.

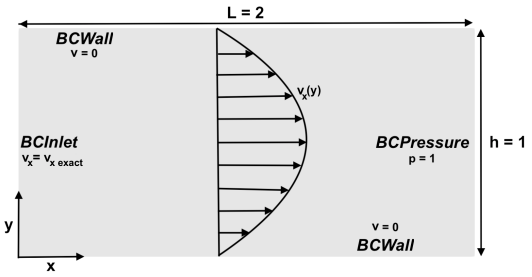

Figure 5: Poiseuille flow: Domain characteristics and boundary conditions.

The analytical solutions of the flow for velocity and pressure are, assuming a pressure gradient of 8μ,

$$v_x(y) = 4hy\left(1 - \frac{y}{h}\right) \tag{2}$$

and

$$p(x) = -8\mu(x - L) + p_{out} \tag{3}$$

where $\mu = 0.1\ \mathrm{kg\,m^{-1}\,s^{-1}}$ is the dynamic viscosity, $h = 1.0$ m the distance between planes, $L = 2.0$ m the domain's length and $p_{out} = 1.0$ Pa the outlet pressure.

To test the SG and OG techniques it is necessary to decompose the domain in at least two sub-grids. Hence, a Circle mesh is used in the center of the domain, with a radius $R = 0.25$. It is able to rotate over its center, to resemble the mesh around a wind turbine's rotor geometry, despite the different orientation with the flow due to it being 2D. In the case of SG, Figure 1, the Domain's sub-grid (red) needed to have a hole cut, so that the Circle mesh (black) could fit. On the other hand, the creation of the OG, in Figure 3, was much simpler, since the Domain grid could be purely cartesian and the Circle mesh was just overlapped on top of it.

Therefore, three different types of sub-grids were created, all of which were systematically refined, with the respective characteristics presented in Table 1. Note that all meshes had the same target cell size in the same refinement level.

Table 1: Poiseuille flow: Description of grid refinements for SG configuration. OG values are not presented since they are similar. Grid refinement h_i calculated based on Domain grid cell count.

Grid	Domain Size	Cell Count (SG)	h_i
G1	20 x 10	249	16
G2	40 x 20	908	8
G3	80 x 40	3 428	4
G4	160 x 80	13 268	2
G5	320 x 160	52 148	1

Concerning the numerical setup, second order accurate discretization of the convection and diffusive fluxes (Central Differences) and time (Implicit Three Time Level) were adopted. Finally, based on an iterative study, the L_∞ norm of the residuals of all flow quantities are reduced at least until 10^{-9} at each time step. This yields the iterative error, compared to the discretization one, negligible.

3.2. Wind Turbine Manufactured Solution

The second test includes the design of a Manufactured Solution resembling a wind turbine flow. It is novel since nothing similar could be found in the literature. The NREL 5MW wind turbine geometric properties and operating conditions were used as reference [9], including the rotor radius, $R_a = 63\,\mathrm{m}$, the rated wind speed, $v_0 = 11.4\,\mathrm{m\,s^{-1}}$, and the rated blade tip speed $80\,\mathrm{m\,s^{-1}}$. In fact, an Actuator Disk simulation was first executed in ReFRESCO with that data, to obtain a flow solution to aid the design process. In Figure 6 the axial velocity distribution of that simulation is presented.

Bearing in mind that issues with velocity fields not respecting continuity led to non-converging CFD simulations in ReFRESCO, the final process of designing those fields needed to take that into consideration. Starting with the axial velocity field, v_z, based on an iterative procedure various primitive functions were tested, having obtained the following equation to replicate the main flow features of Figure 6,

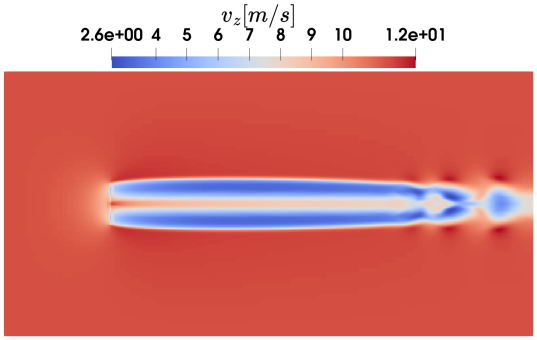

Figure 6: Wind Turbine MMS: Actuator Disk solution, based on NREL 5MW [9], to serve as a reference in the design process. Axial velocity using the G4 refinement of the Domain mesh.

$$\begin{aligned} v_z(r,z) = v_0 &- 0.2715 \cdot v_0 \cdot \gamma_z(z, 0.7, 4.0) \cdot \gamma_r(r, 1.2) \\ &+ 0.2000 \cdot v_0 \cdot \gamma_z(z, 0.7, 4.0) \cdot \gamma_r(r, 2.5) \\ &- 0.1000 \cdot v_0 \cdot \gamma_z(z, -2.0, 1.0) \cdot \gamma_r(r, 3.0) \end{aligned} \tag{4}$$

where $v_0 = 11.4\,\mathrm{m\,s^{-1}}$ is the free-stream velocity. Moreover, the blending functions

$$\gamma_z(z, a, b) = \frac{1}{1 + e^{(\frac{z}{R_a} + a) \cdot b}} \tag{5}$$

and

$$\gamma_r(r, c) = e^{\left(-c \cdot \frac{r}{R_a}\right)^2} \tag{6}$$

where used and tunned to model the velocity field, where $R_a = 63$ m is the actuator disk/rotor radius.

In order to respect mass conservation, the continuity equation in cylindrical coordinates is rearranged. Assuming that the flow is axisymmetric, $\frac{dv_\theta}{d\theta} = 0$, one obtains an expression for the radial component of the velocity field from an integral of the axial velocity previously defined,

$$v_r = \frac{1}{r}\left(\int_0^r -r\frac{\partial v_z}{\partial z} dr\right). \tag{7}$$

While being a straightforward procedure, note that this was a large constraint in the design process, since Sympy, the Python's symbolic toolbox used, was not capable of computing the analytical solution of the integral if the v_z equation was too complex.

Having defined the velocity field, only pressure is still missing. However, no equation exists explicitly relating velocity and pressure for incompressible flows. Therefore, the Bernoulli's Principle is used,

$$p(r,z) = H(r,z) - \frac{1}{2}\rho v(r,z)^2 \tag{8}$$

in which an equation from pressure, p, can be directly extracted if a field of total pressure, H, is also defined. Given the flow properties (incompressible, steady and inviscid), it can be assumed that the free-stream total pressure, H_0, will remain constant all over the domain, except in the wake region, since energy is being extracted from the fluid. By dimensional analysis, that total pressure drop, ΔH, can be estimated as

$$\Delta H = \frac{\Delta P}{Q_{disk}} \tag{9}$$

where ΔP is the harvested power, and Q_{disk} the flow rate of the fluid passing through the turbine's disk. Both these properties can be numerically calculated from the velocity field already defined. Afterwards, having calculated both H_0 and $H_{wake} = H_0 + \Delta H$, they can be blended over the domain,

$$\begin{aligned} H(r,z) = &(H_0 \cdot (1 - \gamma_z(z, 0.0, 4.0)) + \\ &+ H_{wake} \cdot \gamma_z(z, 0.0, 4.0)) \cdot \gamma_r(r, 1.2)) + \\ &+ H_0 \cdot (1 - \gamma_r(r, 1.2)) \end{aligned} \tag{10}$$

from which an equation for pressure can be obtained by applying Equation (8). In Figures 7, 8 and 9 the distribution of axial velocity, radial velocity and pressure over the domain are presented. Note that the harvested power, ΔP, was calculated at 5.008 MW by numerical integration, very close to the rated power of the NREL 5MW, used as reference.

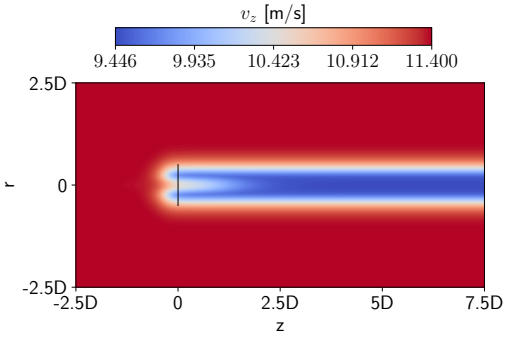

Figure 7: Wind Turbine MMS: Manufactured solution of axial velocity, v_z.

Regarding the cylindrical domain dimensions, they were defined based on the NREL 5MW rotor diameter, $D = 2R_a = 126$ m, as presented in Figure 10. As for the adopted boundary conditions, they were all based on the manufactured solution, i.e. the flow's exact solution. The inlet, on the left of the domain, is of Dirichlet type, whereas the outlet on the right and the sides, on the top and bottom of the domain, are of Neumann type.

Similarly to the Poiseuille flow, three types of sub-grids were created, to enable the use of SG and OG, as exemplified in Figure 11. Note that the Rotor grid was dimensioned to encompass the actuator disk/rotor region, with origin at $(r, z) = (0, 0)$.

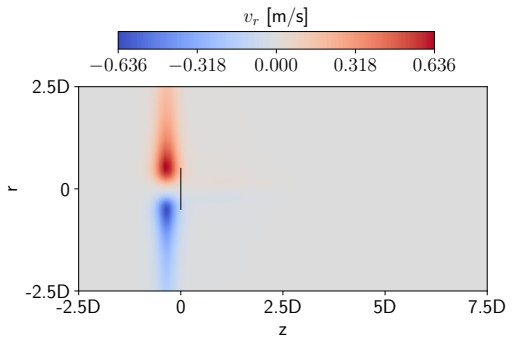

Figure 8: Wind Turbine MMS: Manufactured solution of radial velocity, v_r.

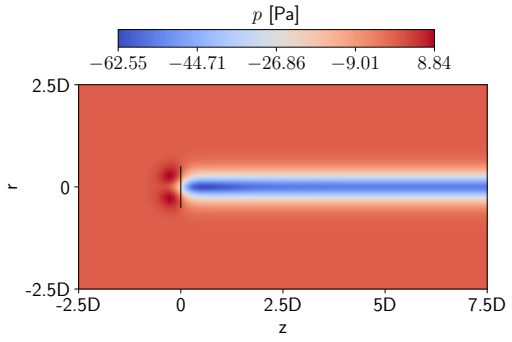

Figure 9: Wind Turbine MMS: Manufactured solution of pressure, p.

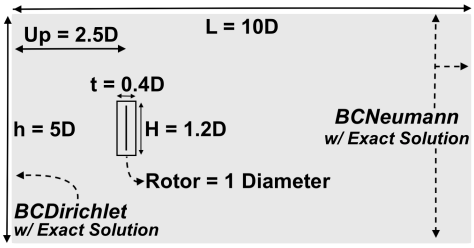

Figure 10: Wind Turbine MMS: Domain dimensions and boundary conditions.

Additionally, to perform Code Verification, a set of four refinements was performed to each sub-grid, as presented in Table 2.

Finally, the numerical setup was similar to the Poiseuille flow, except for the adopted discretization scheme of the convective fluxes, which in this case is upwind-biased: the Limited QUICK. Nevertheless, it is still second order accurate. Moreover, the L_∞ residuals for all flow quantities were reduced up until at least 10^{-6} at all time steps, which was found to yield the iterative error negligible. The default time step is equal to 1.09956×10^{-1} s. This value is such that the Rotor mesh advances 8 degrees per time step, assuming a constant operating angular speed of $1.2698\,\mathrm{rad\,s^{-1}}$, based on the rated

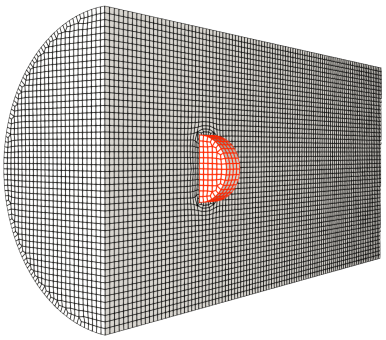

Figure 11: Wind Turbine MMS: Example of SG configuration. Rotor mesh (red) fitted into Domain w/ hole grid (black). G1 refinement.

Table 2: Wind Turbine MMS: Description of grid refinements for SG configuration. OG values are not presented since they are similar.

Grid	Domain Size	Cell Count (SG)	h_i
G1	100 x 50 x 50	0.205 M	2.48
G2	150 x 75 x 75	0.685 M	1.66
G3	200 x 100 x 100	1.608 M	1.25
G4	250 x 125 x 125	3.131 M	1.00

operating condition of the NREL 5MW.

3.3. Wind Turbine NREL 5MW

The final test case consists of the aerodynamic simulation of the rotor geometry of the NREL 5MW wind turbine. It is based on the rated operating condition on [9], the same one considered in the last test case. While no analytical solution exists to perform Code Verification, it is still possible to apply Solution Verification. The main goal is to compare the methods in a realistic scenario. In Figure 12 the adopted domain dimensions are presented, including the boundary conditions.

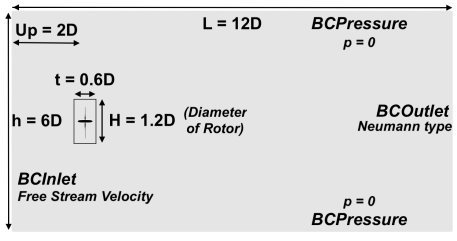

Figure 12: Wind Turbine NREL 5MW: Domain dimensions and boundary conditions.

The meshes around the rotor geometry were generated using the CAD files from [13]. Cell count was kept low, in order to reduce the computational cost, since the main goal was not to obtain accurate aero-

dynamic data, but only compare the grid methods. To achieve that the dimensionless nominal distance to the wall of the first layer of cells of the prism layer, y^+, was kept on average at 35, so that wall functions can be used to solve the boundary layer.

Similarly to the last two test cases, three types of sub-grids were created: Domain, Domain with Hole and Rotor meshes. An example of the SG grid configuration is presented in Figure 13. Each had three grid refinements performed, with their characteristics presented in Table 3.

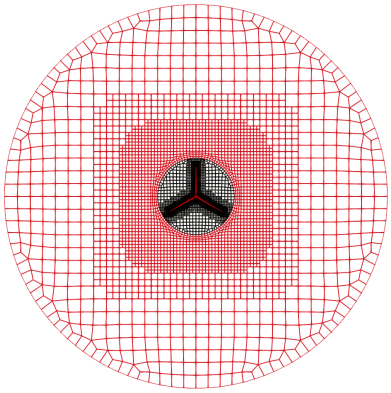

Figure 13: Wind Turbine NREL 5MW: Example of SG configuration. Front view of Rotor mesh (black) fitted into Domain w/ hole grid (red). G1 refinement.

Table 3: Wind Turbine NREL 5MW: Description of grid refinements for SG configuration. OG values are not presented, since they are similar.

Grid	Domain Size	Cell Count (SG)	h_i
G1	80 x 40 x 40	3.789 M	1.39
G2	100 x 50 x 50	6.523 M	1.15
G3	120 x 60 x 60	9.931 M	1.00

Regarding the adopted numerical setup, it was the same as the MMS test case. Additionally, since turbulence is included this time, the two-equation model $k - \sqrt{k}L$ is used due to its stability in these simulations. Concerning the residuals, the L_2 norms of all flow quantities were able to be reduced until stagnation at each time step: worst case occurred in grid G1 for axial velocity, v_x, which was only reduced up to 10^{-3}. Yet, an iterative error study was not performed to evaluate their impact.

4. Results

Given the large number of parameters tested, focus will only be provided to interpolation schemes and their relation to mass imbalance. This parameter is of utmost importance, since it in known to induce pressure fluctuations in incompressible flows, due to their link with mass in the pressure correction equation.

In the case of unsteady quantities, the Transient Scanning Technique [14] was used to assess the statistical uncertainty of the averages obtained. Throughout this work that uncertainty was always kept at least two orders of magnitude lower than the calculated mean quantity by using long enough simulation times.

4.1. Poiseuille Flow

All interpolation schemes presented in Section 2.4 were tested in this test case, ranging from first to third order accurate schemes: NC1, ID1, NCG2, LS2 and LS3 (note that the number in the end represents the scheme's order). In Figures 14 and 15 the grid refinement plots of the pressure errors are presented for both SG and OG, respectively, for all interpolation schemes. They are compared with a single cartesian grid test case, the Baseline.

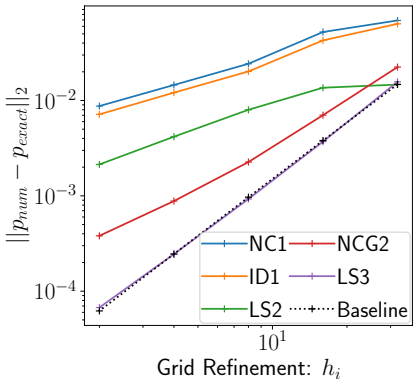

Figure 14: Poiseuille flow: Pressure errors L_2 norm vs. grid refinement. Interpolation schemes with SG. Baseline order of convergence is $p_{ac} = 1.97$.

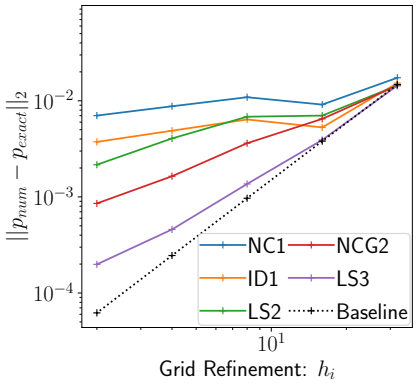

Figure 15: Poiseuille flow: Pressure errors L_2 norm vs. grid refinement. Interpolation schemes with OG. Baseline order of convergence is $p_{ac} = 1.97$.

A clear correlation exists between low order in-

terpolation schemes and higher pressure errors with low orders of convergence (less steep slopes). In fact, the interpolation scheme that best recovered the Baseline order of convergence was the LS3 with SG, which is third order accurate. On the other hand, OG presented a tendency of performing not as well as SG, including with the LS3 scheme. Moreover, note that all errors in grid G1 matched the Baseline results in Overset. This was caused by lack of Fringe cells on the Domain grid, which led to no interpolation errors being transmitted to it. Other flow quantities, as velocity, presented very similar behaviors.

In Figure 16, the mass imbalance, as a percentage of the total mass flow rate passing through the Circle mesh, is presented over a full rotation.

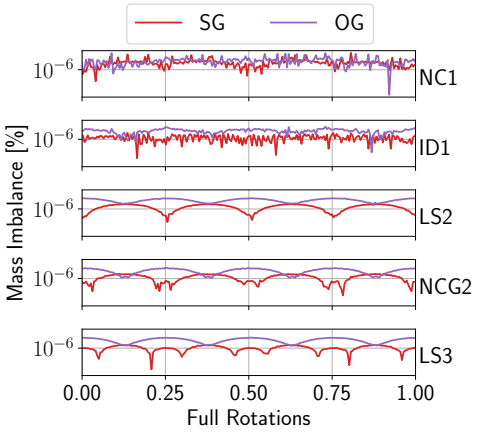

Figure 16: Poiseuille flow: Mass imbalance vs. full rotation of the Circle grid. Mesh G5. Mass imbalance as percentage of mass flow rate going through the Circle grid.

Overall, the amount of mass imbalance is very small, yet still orders of magnitude higher than what would be expected when continuity is respected: around 10^{-13} as perceived in the Baseline. The average mass imbalance tends to be slightly smaller with SG when compared with the same case in OG. Nevertheless, the mean mass imbalance does not appear to depend on the order of accuracy of the interpolation schemes. Instead, the spurious oscillations perceived appear to depend on it, with the schemes of second order or higher having a smoother mass imbalance history.

Considering that the order of accuracy of the methods is driving most of the conclusions obtained, the next test case will focus only on the best interpolation scheme for each order: ID1, NCG2 and LS3.

4.2. Wind Turbine Manufactured Solution

Bearing in mind the results obtained in the previous test case, only three interpolation schemes were tested. Once again, a grid refinement was performed, with ID1 having poor convergence trends and high errors for all flow quantities. On the other hand, NCG2 performed very similarly to LS3 this time, recovering the order of convergence of the Baseline test case (single grid) without any significant amount of errors introduced. This reinforces the importance of the MMS, since the Poiseuille flow conditions are very different from a wind turbine flow (low vs. high Reynolds number), leading to potential misleading conclusions for the target application with only the first test case. In Figure 17 a zoomed-in region near the Rotor grid is presented, with the errors of axial velocity, v_z, being plotted in log scale.

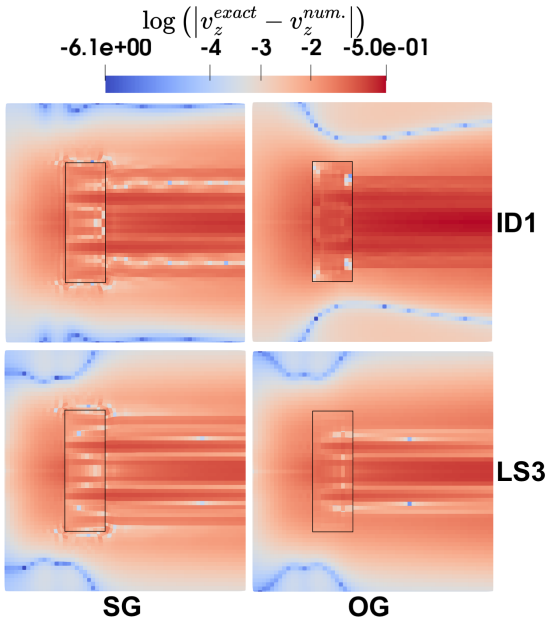

Figure 17: Wind Turbine MMS: Errors of axial velocity, v_z, in log scale. Zoomed-in view near the Rotor grid region. Top row is ID1, bottom row is LS3. First column is SG, second column is OG.

First of all, it is visually confirmed that axial velocity errors are higher when using a first order accurate scheme, ID1, specially in OG. On that matter, NCG2 and LS3 presented very similar results. The errors originate in the Rotor region due to the inter-grid communication process, and are convected downstream, since this is a convection dominated flow. Yet, it is perceivable a thinner wake of errors in OG. This phenomenon is related to the information transfer mechanism, which in SG occurs always at the interface, whereas in OG it depends on the Fringe cell placement, which in this case are more concentrated inside the Rotor mesh.

Next, the mass imbalance, as a percentage of the mass flow rate passing through the Rotor, can be analyzed in Figure 18. Once again, the mass

imbalance introduced is relatively small, however, this time, a relation can be perceived, with higher order interpolation schemes having normally lower amounts of mass imbalance. Yet, this is not general, since the NCG2 with SG has actually a higher value than with ID1. Moreover, the data presented non-monotonic behaviour with grid refinement, so further conclusions would require finer grids to be tested.

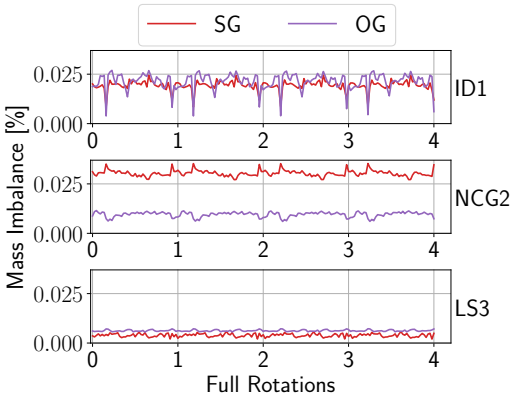

Figure 18: Wind Turbine MMS: Mass imbalance vs. rotations of the Rotor grid. Mass imbalance as percentage of mass flow rate going through the Rotor grid.

Nevertheless, the same trend between order of accuracy of the interpolation schemes and spurious oscillations of mass imbalance is verified once again. These in turn are related to the pressure spurious oscillations verified. For some applications, as acoustics, cavitation and free-surfaces, these can be highly undesirable, since the absolute value of the pressure is crucial.

4.3. Wind Turbine NREL 5MW

Only one time step was tested, equal to 1.09956×10^{-1} s, such that the rotor advances 8 degrees per each time step as in the MMS test case; and one interpolation scheme, LS3, to reduce the number of simulations. However, issues with stability of Overset led to the adoption of half the time step in that case - still, only grid G1 converged. The same time step was tested with grid G1 in SG, with no significant differences perceived. In Figure 19 the mass imbalance values over the last four full rotations of the rotor are presented.

For the case of SG the mass imbalance is less that 1%, with a peak per rotation. With grid refinement the mean value also decreases and so do the peaks. On the other hand, the grid G1 for Overset presented a higher mass imbalance ($> 2\%$) with large spurious oscillations. This could be related to the convergence issues faced in Overset and being caused by the information transfer mechanism

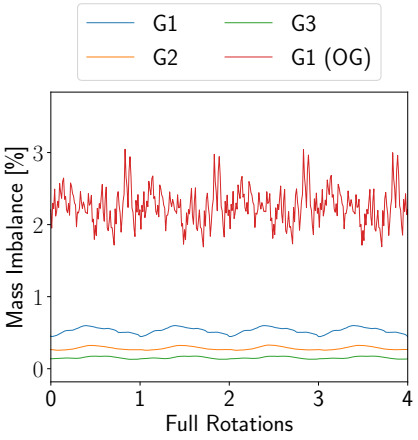

Figure 19: Wind Turbine NREL 5MW: Mass imbalance as a percentage of the mass flow rate passing through the rotor. SG, except for red curve, which is related to grid G1 with OG.

transfering multiple times between sub-grids a given flow particle, thus accumulating interpolation errors. Moreover, the pressure variation over time was surveyed at multiple points, as presented in Figure 20. All probe points are radially located near the same position as the interface ($r_{probe} = 0.595D$, while $r_{interface} = 0.6D$).

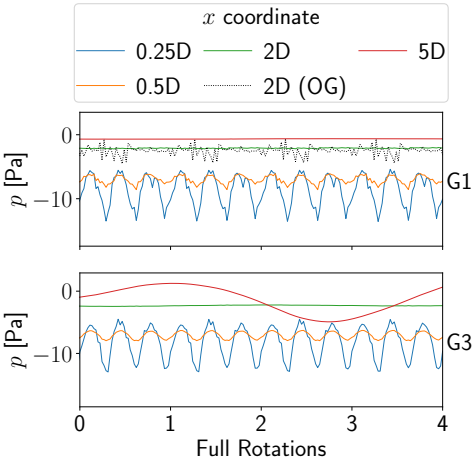

Figure 20: Wind Turbine NREL 5MW: Pressure over last four rotor rotations with SG, measured at $(y, z) = (0, 0.595D)$. Top row: G1. Bottom row: G3. Points with higher x are further downstream in the wake. Black dotted line is one OG computation.

The blue curve, which oscillates three times per rotation due to the number of blades, represents the pressure in a point inside the rotor grid and suggests minor differences between grid refinement G1 and G3. However, the point immediately after, already outside the rotor grid, presents less spurious oscillations in grid G3 than G1. Nevertheless, it is difficult

to relate this directly to possible mass imbalance influence, due to the fact that discretization errors also exist. In fact, the large pressure oscillation perceived at $5D$ represents some vortex-shedding that was captured with grid G3, but not with grid G1. Nonetheless, comparing one of the OG computations (black dotted line) with the equivalent one in SG (green line), clear pressure fluctuations are perceived in OG, congruent with the spurious oscillations verified before in mass imbalance. Therefore, in the case of SG, those same oscillations might exist, but are minimal with the parameters selected.

5. Conclusions

Based on the results obtained, it is perceptible the impact that the interpolation schemes can have on the solution's accuracy. On that matter first order accurate schemes are not recommended, to avoid additional error sources due to interpolation. In fact, the third order accurate scheme, LS3, appears to be the best option among the ones tested, given the low pressure oscillations perceived in the MMS and the NREL 5MW computations with SG.

At this stage, the results seem to indicate that SG are recommended over OG to be used in the CFD simulation of wind turbine rotors, considering the overall reduced quality of the solutions obtained with OG and the difficulties faced in setting up and running the simulations with it. Yet, future work should focus on comparing these results with SG implementations that respect continuity, in order to further assess the impact of mass imbalance in the solution.

Acknowledgements

The author would like to thank Sébastien Lemaire and Guilherme Vaz for their supervision in the development of this work. The use of WavEC's and blueOASIS' facilities and computational resources in the completion of this work are also acknowledged.

References

[1] M. M. Rai. A conservative treatment of zonal boundaries for Euler equation calculations. In *22nd Aerospace Sciences Meeting*, Reno, NV, U.S.A., Jan. 1984. American Institute of Aeronautics and Astronautics.

[2] G. Vaz, P. Quetey, and J. Brunswig. D31.3 Comparison and validation of various mesh coupling strategies. Technical report.

[3] J. Benek, J. Steger, and F. Dougherty. A flexible grid embedding technique with application to the Euler equations. In *6th Computational Fluid Dynamics Conference Danvers*, Danvers,MA,U.S.A., July 1983. American Institute of Aeronautics and Astronautics.

[4] S. Lemaire, G. Vaz, M. Deij - van Rijswijk, and S. R. Turnock. On the accuracy, robustness and performance of high order interpolation schemes for the overset method on unstructured grids. *International Journal for Numerical Methods in Fluids*, Sept. 2021.

[5] T. T. Tran and D.-H. Kim. A CFD study of coupled aerodynamic-hydrodynamic loads on a semisubmersible floating offshore wind turbine. *Wind Energy*, 21(1):70–85, Jan. 2018.

[6] M. M. Rai. Navier-stokes simulations of rotor/stator interaction using patched and overlaid grids. *Journal of Propulsion and Power*, 3 (5):387–396, Sept. 1987.

[7] B. François, M. Costes, and G. Dufour. Comparison of chimera and sliding mesh techniques for unsteady simulations of counter rotating open-rotors. In *XX International Symposium on Air Breathing Engines 2011*, volume 1, pages 520–539, Gothenburg, Sweden, Sept. 2011.

[8] L. Eça and M. Hoekstra. Verification and validation for marine applications of CFD. *International Shipbuilding Progress*, 60:107–141, Jan. 2013.

[9] J. Jonkman, S. Butterfield, W. Musial, and G. Scott. Definition of a 5-MW Reference Wind Turbine for Offshore System Development. Technical Report NREL/TP-500-38060, 947422, Feb. 2009.

[10] G. Vaz, F. Jaouen, and M. Hoekstra. Free-surface viscous flow computations: Validation of URANS code FreSCo. In *Proceedings of the ASME 2009 28th International Conference on Ocean, Offshore and Arctic Engineering*, Volume 5: Polar and Arctic Sciences and Technology; CFD and VIV, pages 425–437, May 2009.

[11] P. J. Roache. *The Method of Manufactured Solutions for Code Verification*. Springer International Publishing, 2019.

[12] S. Lemaire. PyMMS, Jan. 2021. DOI: 10.5281/zenodo.4428181.

[13] M. Make and G. Vaz. Analyzing scaling effects on offshore wind turbines using CFD. *Renewable Energy*, 83:1326–1340, Nov. 2015.

[14] J. Brouwer, J. Tukker, and M. van Rijsbergen. Uncertainty analysis and stationarity test of finite length time series signals. In *4th International Conference on Advanced Model Measurement Technologies for the Maritime Industry*, Sept. 2015.